Christian Morsbach
First *Last*

ASME Paper Title: Investigating the Unsteady Dynamics of a Multi-Jet Impingement Cooling Flow Using Large Eddy Simulation

Authors: Christian Morsbach, Marcel Matha, Robin G. Brakmann, Sadiya Tabassum, Michael Bergmann, Michael Schroll, Christian Willert, Edmund Kügeler

ASME Journal Title: Journal of Turbomachinery

Volume/Issue 147 (3) Date of Publication (VOR* Online) 8 October 2024

ASME Digital Collection URL: https://asmedigitalcollection.asme.org/turbomachinery/article/147/3/031002/1206153/Investigating-the-Unsteady-Dynamics-of-a-Multi-Jet

DOI: https://doi.org/10.1115/1.4066508

Christian Morsbach[1]
Institute of Propulsion Technology
German Aerospace Center (DLR)
Linder Höhe, 51147 Cologne, Germany
email: christian.morsbach@dlr.de

Marcel Matha
Institute of Propulsion Technology
German Aerospace Center (DLR)
Linder Höhe, 51147 Cologne, Germany

Robin G. Brakmann
Institute of Propulsion Technology
German Aerospace Center (DLR)
Bunsenstrasse 10, 37073 Göttingen, Germany

Sadiya Tabassum
Institute of Test and Simulation for Gas Turbines
German Aerospace Center (DLR)
Am Technologiezentrum 5, 86159 Augsburg, Germany

Michael Bergmann
Institute of Propulsion Technology
German Aerospace Center (DLR)
Linder Höhe, 51147 Cologne, Germany

Michael Schroll
Institute of Propulsion Technology
German Aerospace Center (DLR)
Linder Höhe, 51147 Cologne, Germany

Christian Willert
Institute of Propulsion Technology
German Aerospace Center (DLR)
Linder Höhe, 51147 Cologne, Germany

Edmund Kügeler
Institute of Propulsion Technology
German Aerospace Center (DLR)
Linder Höhe, 51147 Cologne, Germany

Investigating the unsteady dynamics of a multi-jet impingement cooling flow using large eddy simulation

We investigate the unsteady behavior of an in-line jet impingement array of nine jets at a Reynolds number of 10 000 in a narrow channel subjected to a developing cross flow of up to 25% of the bulk jet velocity. To this end, we present an improved version of a previously published large eddy simulation (LES) now with resolved turbulence at the inflow boundaries. After a careful analysis of the transient behavior and statistical convergence of the LES, we discuss the time-averaged heat transfer characteristics of the configuration compared to numerical references of similar configurations. We then show how the large-scale unsteadiness increases from jet to jet. Both space-only and spectral proper orthogonal decompositions (POD and SPOD) are used to discuss the large-scale organization of single jets and multiple jets in combination. The latter shows a qualitative change in the unsteady behavior of the temperature footprint on the impingement wall with increasing cross flow.

Keywords: impingement cooling, large eddy simulation, unsteady analysis, modal decomposition

Nomenclature

Roman letters

D = Pipe or jet diameter [m]
e_N = Statistical error on the mean after N realizations
f = Frequency [Hz]
H = Channel height [m]
L = Length [m]
p = Pressure [Pa]
P = Axial pipe or jet spacing [m]
q = Heat flux magnitude [W m^{-2}]
Q = Q-criterion for vortex visualization [s^{-2}]
r = Cross flow ratio
t = Time [s]
T = Temperature [K]
u, v, w = Cartesian velocity components [m s^{-1}]
V = Volume [m^3]
x, y, z = Cartesian coordinates [m]

Greek letters

Δ = Cell size or length [m]
λ = Thermal conductivity [W m^{-1} K^{-1}]
λ_i = POD or SPOD eigenvalue of mode i
ν = Kinematic viscosity [m^2 s^{-1}]
ϕ = POD or SPOD mode
σ_i = SVD singular value

Dimensionless groups

Ma = Mach number
Nu = Nusselt number
Re = Reynolds number
St = Strouhal number

Superscripts and subscripts

aw = Adiabatic walls

[1] Corresponding Author.
August 5, 2024

bulk = Spatial average over cross section
c = Convective
jet = Jet value
wall = Wall value
rel = Relative value
ref = Reference value
s = Sampling
0 = Stagnation value
$\|$ = Parallel to wall
$+$ = Wall unit

Operators

$\overline{\square}$ = temporal average
$\langle \square \rangle$ = spatial average

1 Introduction

In modern gas turbines engines, the thermodynamic efficiency is affected by the turbine inlet temperature and the compression ratio. Hence, high-pressure turbine blades often face temperatures exceeding their material's melting point. To withstand these conditions, an active cooling system, which utilizes air extracted from the compressor, is mandatory. However, diverting air for cooling reduces the engine's overall efficiency. A commonly used cooling technique for turbine blades is impingement cooling, which typically employs arrays of jets that direct cooling air onto the hot internal surfaces. The efficiency of impingement cooling is crucial, as it directly impacts the overall performance and longevity of high-pressure turbine parts. A major drawback of impingement cooling is the creation of hot spots, resulting in uneven cooling. Introducing periodic variations in the flow can improve its interaction with the hot surface, effectively mitigating the hot spot effect. The flow's unsteadiness disrupts the thermal boundary layer, enhancing heat transfer. Hence, predicting the heat transfer rates in complex cooling systems is difficult and often results in non-optimized designs using too much cooling air. Effectively implementing novel strategies necessitates a comprehensive understanding of the unsteady behavior of jet flow.

In the past, heat transfer analysis primarily focused on steady-state conditions. However, examining the dynamic behavior of the flow can provide a deeper understanding, allowing for strategic alternation of the impingement domain to enhance heat transfer efficiency. A comprehensive overview of basic steady-state physical phenomena and advancements in impingement jet heat transfer over the past decades is documented in several review papers. Recent review papers such as Weigand and Spring [1] and Barbosa et al. [2] describe the flow phenomena and interactions, providing correlations for heat transfer and discussing recent developments regarding heat transfer enhancements. Dutta and Singh [3] specifically focus on heat transfer enhancements, such as the use of ribs and surface obstructions, as well as features that increase the surface area in impingement jet setups, while Plant et al. [4] discuss the literature on both jet impingement and sprays. Comprehensive reviews and evaluations of various numerical methods, such as Reynolds-averaged Navier-Stokes (RANS), Large Eddy Simulation (LES), and Detached Eddy Simulation (DES), for predicting impingement jets, with a particular emphasis on single jet setups, have been presented by Shukla and Dewan [5] and Zuckerman and Lior [6].

There exists rather limited literature on high-fidelity simulations of single-row impingement configurations in narrow channels. While there are Direct Numerical Simulation (DNS) studies on single impinging jets in the relevant Reynolds number regime of $\mathcal{O}(10^4)$ [7,8], configurations involving multiple jets have been investigated in the recent years using LES due to the increased computational effort required to resolve larger domains. Hossain et al. [9] claim to have published the first LES study of such a narrow-channel configuration which was validated with Particle Image Velocimetry (PIV) and Temperature Sensitive Paint (TSP). They simulated 5 jets at a Reynolds number of 15 000 spaced $5D$ (jet diameters) apart, which impinge on a heated plate of width $5D$ at a distance of $3D$, using a second-order accurate commercial flow solver with the subgrid stresses modelled by the wall-adapting local eddy-viscosity (WALE) model. Their simulation resolved a small part of the plenum over the short pipes of one jet diameter length. Not only the impingement wall but also the side walls of the channel were heated with a constant heat flux boundary condition. Both in terms of velocity field and heat transfer they showed consistent results with the experiments. While the channel of Hossain et al. [9] was closed to one end, such that the jets are exposed to a self-generated developing cross flow, Otero-Pérez et al. [10] presented a configuration in which they were able to prescribe defined cross flow profiles as an inlet boundary condition. It consists of 3 jets at a Reynolds number of 10 000 and a Mach number of 0.3, which impinge on a plate with a constant heat flux at a distance of $4.5D$. In their parametric study, they varied the jet spacing with values of $5D$, $10D$ and $15D$ for the case without cross flow and subjected the jets at $10D$ spacing with both laminar and turbulent cross flow boundary layer profiles at different velocities. While they also employed the WALE model for the subgrid stresses, they used an in-house fourth-order accurate finite fifference (FD) solver with skew-symmetric convective fluxes and a filter to avoid numerical oscillations [11]. Since their configuration featured spanwise periodic boundary conditions instead of solid walls, it technically represents a 2D array of jets instead of a single row of jets in a channel. Note, that their spanwise domain size was always equal to the axial jet spacing. Their analysis focused mainly on the influence of the different parameters on the heat transfer in terms of local and spanwise-averaged Nusselt number.

Other recent LES studies are geometrically different from the configuration considered in this paper. Draksler et al. [12] presented an analysis of a hexagonal array of jets at a Reynolds number of 20 000 impinging on a heated plate at a distance of $4D$. They showed that LES was able to reproduce the relevant physical effects such as fountain flow due to wall jet collision and negative production of normal stresses near the impingement wall. In a follow-up paper, Draksler et al. [13] presented an analysis of grid dependence and statistical errors on first and second moments of velocity. Yet another type of configuration was investigated by Nguyen et al. [14]. Here, the cross flow was varied in a pipe feeding a linear array of 7 jets at a Reynolds number of 5 000, which are spaced at $2.25D$ and impinge on a heated flat plate of $20D \times 15D$ mounted at a distance of $3D$ in an even larger domain allowing the jet fluid to expand laterally in a nearly undisturbed manner. Besides the cross flow in the pipe, they also varied the Mach number. They used a lattice Boltzmann method to perform an LES, which they validated against PIV and infrared thermography data. A configuration representative of the cooling scheme within a vane was introduced by Laroche et al. [15] where jets at a mean Reynolds number of 10 000 are directed in to the concave, narrow leading edge region at a distance of $6.4D$ as well as onto flat plates at a distance of $2D$. It was analyzed both experimentally and with a hybrid RANS/LES method implemented in a second-order accurate, unstructured in-house code. The hybrid RANS/LES showed advantages over conventional RANS schemes in terms of heat transfer prediction.

While most of the studies listed above focus on time-averaged results and turbulence statistics, Yang et al. [16] also discuss the unsteady behavior of a single row of 10 jets fed from a plenum with cross flow through pipes of length D, which impinge onto a cylindrical target at a distance of $3D$ and are spaced at $3D$. They investigate the configuration both experimentally with time-resolved surface temperature measurement techniques and numerically using steady and unsteady RANS simulations with a commercial flow solver. While this study included a variation of jet Reynolds number from 10 000 to 20 000, the same authors present a more detailed analysis of the unsteady effects for the Reynolds number of 15 000 [17]. In both papers, they connect the unsteadiness of the jets with a Kelvin-Helmholtz (KH)-like shedding of the cross

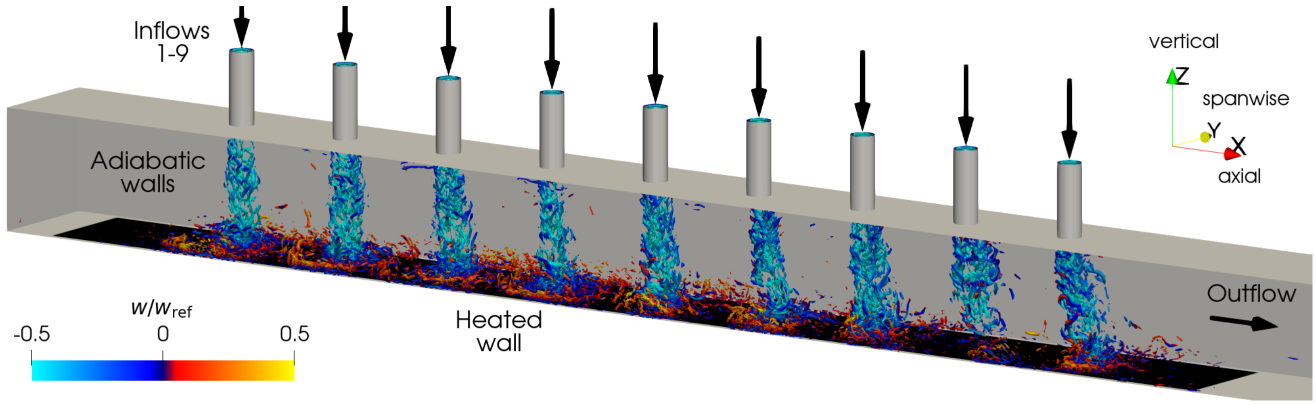

Fig. 1 Computational domain of the LES with heated portion of the wall marked in black and instantaneous turbulent structures for case C1 visualized by isosurface of $QD^2/w_{\mathrm{ref}}^2 = 5$

Table 1 Geometrical properties of the configuration

Pipe diameter	D	0.0152m
Pipe separation	P	$5D$
Pipe length	L_{pipe}	$3D$
Channel height and width	H	$5D$
Heated length	$L_{x,\mathrm{heated}}$	$55D$
Heated width	$L_{y,\mathrm{heated}}$	$4.45D$
Position jet 7	x_{jet7}	0
Closed channel end	x_{end}	$-39.6D$
Outflow	x_{outflow}	$38.8D$

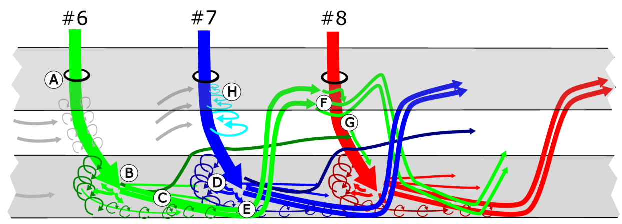

Fig. 2 Schematic of the flow topology focusing on jets 6, 7 and 8 (adapted from [20])

flow downstream of the blockage caused by the jets. Another recent study by Rönnberg and Duwig [18] discusses the unsteady heat transfer and associated flow features in a single impinging jet configuration. The authors demonstrate how modal decomposition techniques can be successfully applied to extract knowledge on the large scale organization in the flow even if the relative energy in these modes is low.

In the present paper, we focus on unsteady effects in a generic configuration of nine cooling jets with a separation of $5D$ in a square channel. The cooling jets with an average Reynolds number based on the jet diameter of 10 000 impinge on a heated plate at a distance of $5D$ with a constant wall heat flux. The configuration is not only realized numerically but has also been set up with good optical access for PIV measurements, which limited the jet bulk Mach number to 0.045. It was initially introduced by Tabassum et al. [19] with a focus on RANS approaches compared to temporally averaged PIV and a baseline LES with a wall heat flux of 5 000 W/m^2. We extend the presentation and discussion of our original LES setup along with a sensitivity study related to the inflow boundary conditions. Therefore, an additional LES is considered, where resolved turbulence is introduced at the previously laminar inflow boundaries. We will investigate the effect of these modified boundary conditions on the development of the cooling jets and their heat transfer characteristics. The primary aspect of this study is our focus on the unsteady behavior of the interacting jets. We will assess the (potential) coupling between adjacent jets and those further apart using modal decomposition techniques. To the best of our knowledge, no modal analyses based on high-fidelity simulations of single-row impinging jets with steady-state inflow can be found in the literature to date. We seek to provide valuable insights necessary for the design of advanced cooling channel geometries targeted at improved efficiency of the cooling system.

2 Numerical setup

The configuration investigated with LES represents a slight modification of the experimental setup as briefly discussed by Tabassum et al. [19]. It consists of nine pipes which feed the jet fluid into a square channel with a heated impingement wall as sketched in Figure 1. Notably, the channel remains closed to the left, exposing the jets to a self-generated, developing cross flow. The geometrical properties of the configuration are summarized in Tableau 1. Note that the origin of the coordinate system is on the heated wall below the center of jet 7.

Figure 2 illustrates the flow dynamics the impingement jet array under self-induced cross flow, specifically focusing on jets 6, 7, and 8. A free jet emerges from the impingement hole, entraining the surrounding fluid (Ⓐ). In the stagnation zone, the fluid encounters an adverse pressure gradient, decelerating its velocity to zero (Ⓑ). Following impingement, the pressure field accelerates the flow radially, leading to the formation of wall jets (Ⓒ). These wall jets collide with those from neighboring impingement jets, creating a fountain flow that ultimately forms a vortex (Ⓓ). The fluid is then displaced towards the side walls by adjacent jets, guiding it along the walls to the hole plate (Ⓔ). A portion of this fluid recycles back into the jet, while the remainder merges with the cross flow, recirculating in a corkscrew movement towards the outlet (Ⓕ). The cross flow significantly deflects the jet's trajectory towards the target, enhancing shear forces and, consequently, reducing the heat transfer (Ⓖ). The cross flow around the jet induces a vortex pair parallel to the impingement jet axis (Ⓗ).

Numerically, the heated wall is realized through a constant heat flux boundary condition, while all other solid walls are treated as adiabatic. At the outflow, a 1D non-reflecting boundary condition based on a characteristics formulation [21] controls the time-averaged pressure, which was determined iteratively to yield the experimental mass flow. The inflow conditions for each jet pipe are extracted from preliminary RANS computations of the configuration including the plenum [19] to be able to account for the non-homogeneous velocity distribution and to reproduce a vena contracta effect. They are prescribed as temporally constant 2D distributions using local Riemann boundary conditions.

We use *TRACE*'s finite volume (FV) method to solve the fil-

Table 2 Simulated operating conditions

Case	C1	C2	C3
$\mathrm{Re}_{\mathrm{jet}}$		10 000	
$\mathrm{Ma}_{\mathrm{jet}}$		0.034 to 0.037	
q_{wall} / Wm^{-2}	5000	5000	2000
Inflow	Laminar	Turbulent	Laminar
$t_{\mathrm{simulation}}/t_{\mathrm{c}}$	1118.9	1072.0	443.7

Table 3 Area-averaged and maximum wall adjacent cell sizes in wall units (reproduced from [19])

Domain location	$\Delta\mathbf{x}_{\parallel}^{+}$ avg	$\Delta\mathbf{x}_{\parallel}^{+}$ max	y_1^+ avg	y_1^+ max
Pipes	15.78	80.13	0.42	1.54
Impinging wall	15.63	79.76	0.41	1.17
Upper wall	9.15	35.49	0.22	1.94
Side walls	14.76	49.96	0.31	0.93

tered compressible Navier-Stokes equations using a second-order accurate, density based scheme applying MUSCL reconstruction with $\kappa = 1/3$ [22] for the convective fluxes. A fraction of 10^{-2} of Roe's numerical flux [23] is added to a central flux to avoid odd-even decoupling. The viscous fluxes are computed using central differences. Time integration is performed using a third-order accurate Runge-Kutta method [24]. The subgrid stresses are computed using the WALE model of Nicoud and Ducros [25]. This solver setup has successfully been used to generate LES data of turbomachinery flows [26–28].

Three different operating conditions have been computed as summarized in Tableau 2. The first case C1 is the same setup as described by Tabassum et al. [19] but with a longer period sampled to allow for the analysis of low-frequency phenomena. Apart from the good agreement of time-averaged data between LES and PIV, Schroll et al. [29] have shown that local unsteady effects extracted from high-speed PIV were reproduced consistently for this case. The cases C2 and C3 represent variations of the boundary conditions. It was expected that missing resolved turbulence might be a reason for the discrepancies between PIV and LES observed in the jet velocity profile reported by Tabassum et al. [19]. Therefore, case C2 introduces resolved turbulence at the inflow boundaries through a Synthetic Turbulence Generator (STG) as proposed by Shur et al. [30], which is supplied with the turbulent kinetic energy and dissipation rate distribution from the preliminary RANS computation. For the sake of completeness, we also list case C3, which was intended to be more closely aligned with measurements using TSP (cf. Schroll et al. [29]) but will not be analyzed in detail in this paper.

The domain is meshed in a block-structured topology as shown for the region around jets 6 and 7 in Figure 3. To ensure an appropriate resolution of the pipe boundary layers, a butterfly topology (OH) was chosen, which extends into the channel and follows the expected jet deflection. Across the pipe, there are 15 cells in the O-block and 30×30 cells in the central H-block. The extended pipe O-blocks are surrounded by another O-block to relax the near wall resolution and the rest of the channel is filled with H-blocks which are appropriately refined towards all solid walls. The z-direction of the square channel is discretized with 210 cells resulting in a total of 6.7×10^7 cells for the entire configuration. As summarized in Tableau 3, the maximum non-dimensional cell sizes of the wall adjacent cells are in line with recommendations for LES [31] while the area-averaged values are well below these guidelines. The grid resolution in the jet shear layers and remaining channel was confirmed to be adequate by comparing the spatial cut-off scale and the estimated Kolmogorov length scale $\Delta_{\mathrm{cut}}/l_\eta = V^{1/3}/\left(\nu^3/\epsilon\right)^{1/4}$ [32].

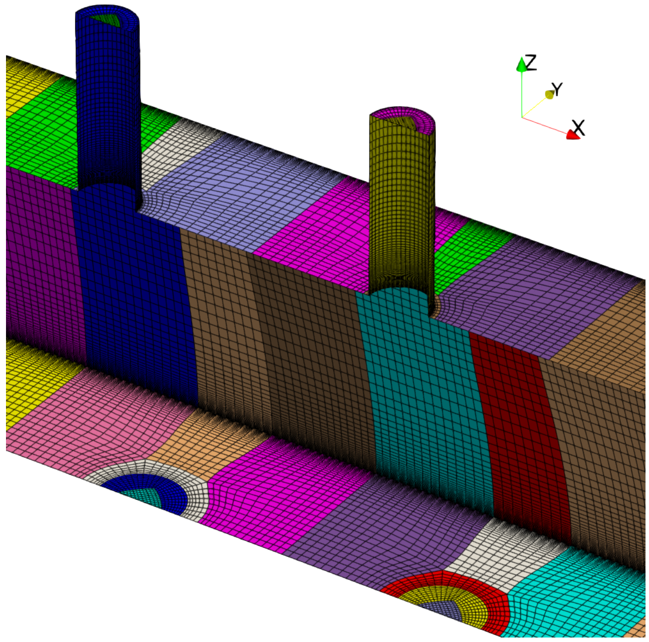

Fig. 3 Details of the computational surface mesh around jets 6 and 7 cut in half at $y = 0$ with two out of five elements shown per index direction. Colors indicate different surface blocks.

In the following, all physical quantities will be normalized using the following set of reference values: the jet diameter D, the maximum vertical velocity w_{ref} and the bulk total temperature $T_{\mathrm{ref}} = T_{0,\mathrm{jet1}}$ of jet 1. We define a convective time scale as $t_{\mathrm{c}} = D/w_{\mathrm{ref}}$. For the current study, we sampled primitive variables and their gradients on the impingement wall of the channel with a resolution of 300×30 and on the $y = 0$ plane of the channel with a resolution of 280×30 at a rate of $f_{\mathrm{s}} t_{\mathrm{c}} = 13.45$. Full 3D solutions allowing for later extraction of spatially higher resolved data were sampled at a rate of $f_{\mathrm{s}} t_{\mathrm{c}} = 5.35$ using *TRACE*'s ParaView Catalyst [33] interface and have also been used in the following analyses if required. In addition to the temporally resolved data sets, statistical moments allowing to obtain the budget terms of the Reynolds stress transport equations were computed online at the full spatial resolution.

Before any averaging or unsteady analysis can be conducted, it has to be ensured that transients from the initialization have been washed out of the domain and statistically steady flow has been established. This is often done by a rather subjective inspection of integral quantities such as mass flows or forces acting on surfaces. We choose to employ the marginal standard error rule (MSER) [34] on the spatially resolved data sets as described in detail by Bergmann et al. [27]. Figure 4 shows the estimated end of the initial transient $t_{\mathrm{transient}} w_{\mathrm{ref}}/D$ for the vertical velocity component w (*top*) on the plane $y = 0$ and for the temperature T on the impingement wall at $z = 0$ (*bottom*) for the case C1. For better orientation, the positions of the pipes are marked on the top axis and as circles, where appropriate, and the mean flow is illustrated as streamlines. At many locations, the MSER determines an end of the initial transient for $t = 0$. This can be explained by the fact that the simulation was restarted from an already existing LES solution after a correction of the inflow boundary conditions. A majority of the locations is marked converged at well below $100 t_{\mathrm{c}}$. Exceptions can be found in the low-speed areas between the jets with the largest values between jets 1 and 2 and between 4 and 5. On the impingement wall, the maximum transient times can be found close to the channel side walls where the heated portion of the wall ends.

A more quantitative analysis of the estimated transient times is presented in Figure 5. At the bottom, we plot the probability

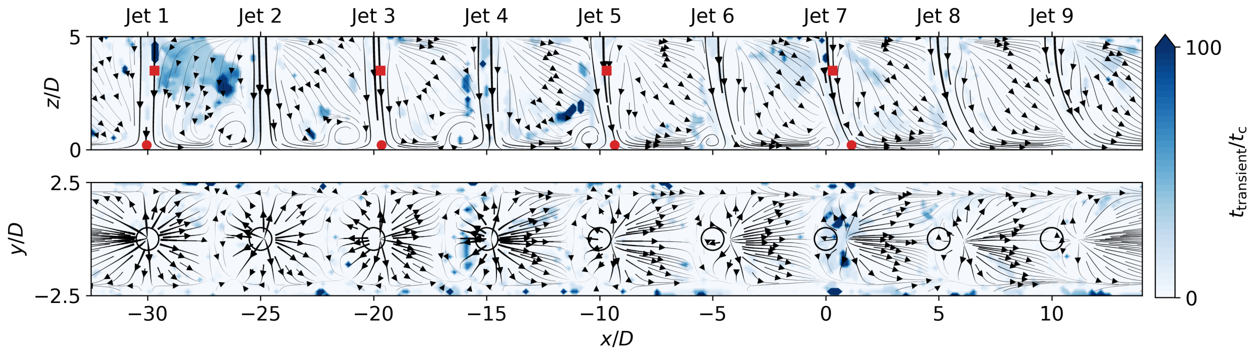

Fig. 4 Transient time computed with MSER (C1) for vertical velocity component *w* on slice at *y* = 0 (*top*) and temperature *T* on heated wall (*bottom*). The mean flow is illustrated with streamlines. Positions where frequency spectra are compute marked with red squares and circles.

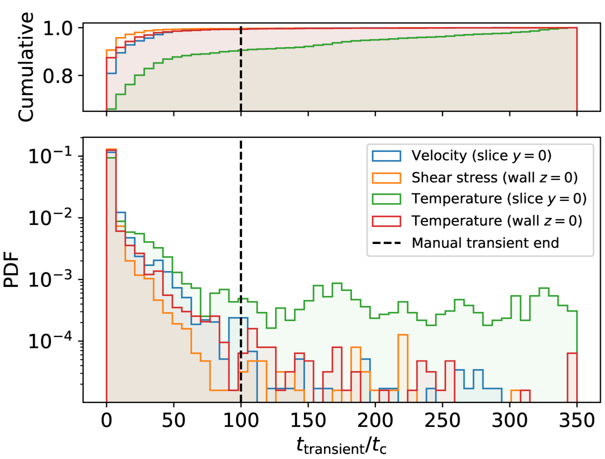

Fig. 5 Statistical analysis of transient times (C1) for velocity *w*, wall shear stress $\tau_{w,x}$ and temperature *T* on slice at *y* = 0 and heated wall with probability density function (*bottom*) and cumulative area fraction of transient below given time (*top*)

density function (PDF) of the transient end times over the two subdomains shown in Figure 4 with additional information about the temperature on the $y = 0$ plane and the shear stress on the impingement wall, while the top panel shows the cumulative fraction of transient end times smaller than the current. The shear stress on the impingement wall is the fastest converging quantity with roughly 90% of the time signals showing statistical convergence according to the MSER before $7t_c$. The temperature on the wall and the velocity in the $y = 0$ plane follow a similar trend in the PDF and by $100t_c$ 99.5% of the time signals have converged. Only the temperature in the $y = 0$ plane shows slightly slower convergence. After a similarly steep decay in the PDF until $50t_c$, the rate at which more time signals converge becomes considerably slower and only 92.7% of the signals show statistical convergence after $100t_c$. We set our global end of transient to $100t_c$ since we do not evaluate this particular quantity in further analyses. Nevertheless, we consider it worthwhile showing this behavior as it should raise awareness about the intricacies of initial transient detection.

3 Time-averaged results

To put our later discussion of the unsteady dynamics into a perspective, we start with an analysis of the heat transfer on the impingement wall. The temperature distribution on the wall can be written in terms of a Nusselt number

$$\mathrm{Nu}(x, y) = \frac{q_{\text{wall}}(x, y) D}{\lambda(x, y)\,(T_{\text{wall}}(x, y) - T_{\text{ref}})} \tag{1}$$

with the local thermal conductivity $\lambda(x, y)$, the local wall temperature $T_{\text{wall}}(x, y)$ and a reference temperature T_{ref}. The latter would ideally be taken as the local adiabatic wall temperature $T_{\text{aw}}(x, y)$, requiring another simulation with $q_{\text{wall}} = 0$. At low Mach numbers, the reference temperature is typically chosen as $T_{\text{ref}} = T_{0,\text{jet}}$ [35], which, as Otero-Pérez and Sandberg [11] argued, might not be a good choice. To assess the influence of the choice of T_{ref} in our case, we extrapolated $T_{\text{aw}}(x, y)$ using the two laminar inflow simulations with different wall heat fluxes C1 and C3 [11]. The resulting Nusselt number distribution yielded negligible differences to the one obtained with $T_{\text{ref}} = T_{0,\text{jet}}$. Therefore, we can refrain from running another simulation to obtain $T_{\text{aw}}(x, y)$ for the turbulent inflow case. This is in line with the reasoning by Nguyen et al. [14], who decided against a scaling of the case to a higher Mach number because that would invalidate the choice of $T_{\text{ref}} = T_{0,\text{jet}}$.

Figure 6 shows the time-averaged Nusselt number distribution (*top*) on the impingement wall for the laminar inflow case C1. The relative 68% confidence interval (CI) of the mean (*bottom*) was computed following the method described by Bergmann et al. [27]. While the mean value was computed from the online time average at full spatial resolution, the CI has to be computed from the full time series, which was sampled at reduced spatial resolution as described above. Note that the lateral bounds of the heated area can be identified by values of $\overline{\mathrm{Nu}} = 0$ close to the channel side walls. The CI is only shown for the heated area. The distribution of the mean has already been discussed in detail by Tabassum et al. [19]. Generally, the increasing cross flow can be seen to move the impingement point of the jets downstream and change the shape of the high Nusselt number area under the jet from circular to a crescent moon shape. Secondary maxima between the jets can be attributed to the recirculation resulting from the colliding wall jets which brings colder fluid down to the wall, cf. Nguyen et al. [14].

The relative CI increases with increasing cross flow from left to right. For each jet, the largest relative errors can be found in the regions of the colliding wall jets and the interaction with channel side wall. With increasing cross flow, this region with large error moves downstream towards the impingement area of the respective jet until it nearly coincides with the stagnation point in jet 9. This is already a hint towards larger scale unsteadiness compared to jet 1, which basically contains only small scale turbulence leading to small CI values. While the average CI is at roughly 1.8%, the maximum values of 6% can be found under jet 8. We will later exclude jets 8 and 9 from the unsteady analysis to avoid boundary effects.

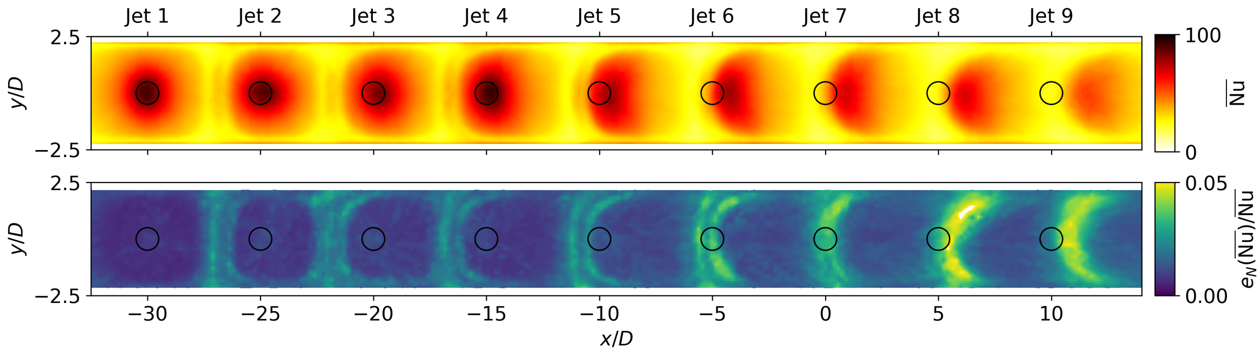

Fig. 6 Time-averaged Nusselt number and relative 68% confidence interval on heated wall for laminar inflow case C1

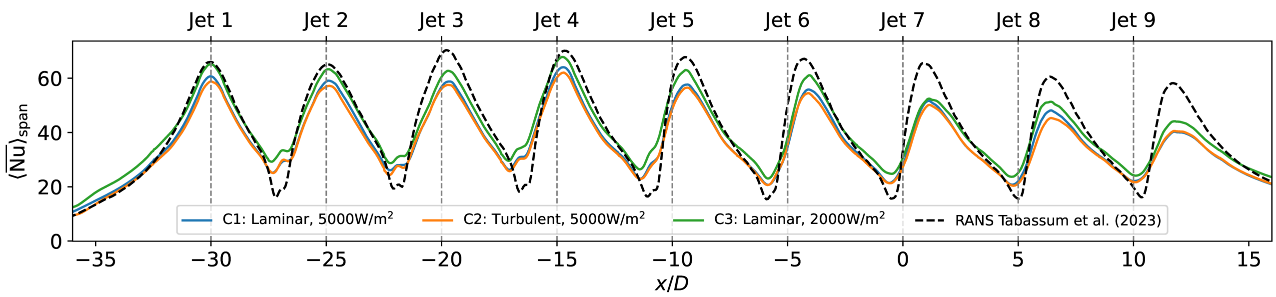

Fig. 7 Comparison of time- and spanwise-averaged Nusselt number $\langle\overline{\mathrm{Nu}}\rangle_{\mathrm{span}}$ on heated wall

For a quantitative comparison of the three computed cases, we show the time- and spanwise-averaged Nusselt number $\langle\overline{\mathrm{Nu}}\rangle_{\mathrm{span}}$ for the three cases compared with the RANS results of Tabassum et al. [19][2] in Figure 7. RANS generally overestimates the heat transfer maxima in the jet stagnation regions due to excessive production of turbulent kinetic energy [19] and predicts the Nusselt minima slightly further downstream than the LES. The differences between the LES results are subtler. Cases C1 and C2 produce nearly identical results with the exception that the heat transfer in the jet stagnation region is slightly larger for the laminar inflow case than for the turbulent inflow case. This can be explained by less turbulence in the initial shear layers of the jet leading to a reduced mixing with the surrounding fluid and thus larger potential core of the jet. The magnitude of this variation is even lower than the variation due to the change in heat flux boundary condition, which was deemed as minor by Tabassum et al. [19].

Figure 8 shows the jet deflection defined as relative downstream shift of the Nusselt number maximum $(x_{\mathrm{Nu}_{\max}} - x_{\mathrm{jet}})/D$ over the relative bulk cross flow velocity $\langle\overline{u}\rangle_{\mathrm{bulk,channel}}/\langle\overline{w}\rangle_{\mathrm{bulk,jet}}$. A jet with no deflection will give $(x_{\mathrm{Nu}_{\max}} - x_{\mathrm{jet}})/D = 0$ as it is found for jet 1 in all computations. The bulk cross flow velocity is computed as an area average over the square channel at a position $2.5D$ upstream of the respective jet center. All three LES show practically the same behavior and we only plot cases C1 and C2 for a clearer presentation. Two distinct ranges of linear relation between the jet deflection and cross flow ratio can be observed for both cases. After an initial slow increase in jet deflection at low cross flow ratios, it increases more rapidly from jet 4 onward with higher cross flow ratios. The RANS results [19] on the other hand show a more varying slope along the nine jets.

To put our results into perspective, we also included the jet deflection derived from Otero-Pérez et al. [10] Fig. 5(a) for both

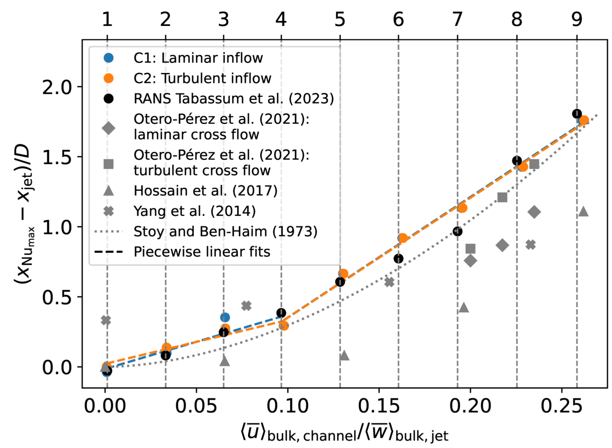

Fig. 8 Jet deflection over cross flow for cases C1 and C2 in comparison with numerical [9,10,19] and experimental [36] references in rectangular channels and experimental results with a cylindrical impingement target [16]

laminar (diamonds) and turbulent cross flow (squares).[3] Note that their channel height and width are $4.5D$ and $10D$, respectively, and that they have used periodic boundaries in the spanwise direction. Furthermore, in contrast to our simulations upstream of jet 7, their initial cross flow does not contain any secondary flow motions and

[2]Compared to Tabassum et al. [19], who used a constant thermal conductivity, we recomputed the Nusselt number using Equation (1) with the local thermal conductivity.

[3]The cross flow ratio downstream of the n^{th} jet was estimated assuming incompressible flow as

$$r(n) = r_0 + \frac{n\pi D^2}{4HL_y}$$

with $H/D = 4.5$, $L_y/D = 10$ and the initial cross flow ratio $r_0 = 0.2$.

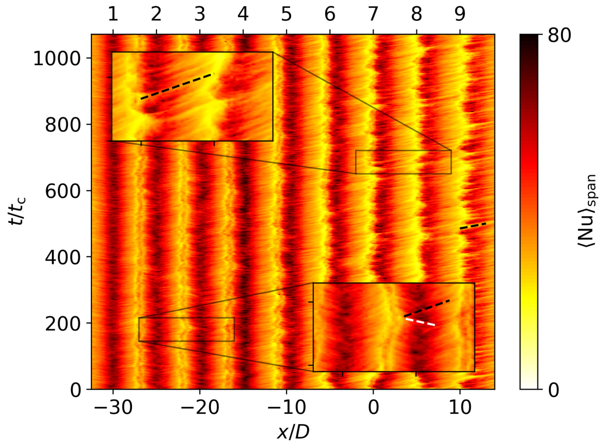

Fig. 9 Temporal evolution of spanwise-averaged Nusselt number $\langle \mathrm{Nu} \rangle_\mathrm{span}$ for the turbulent case C2

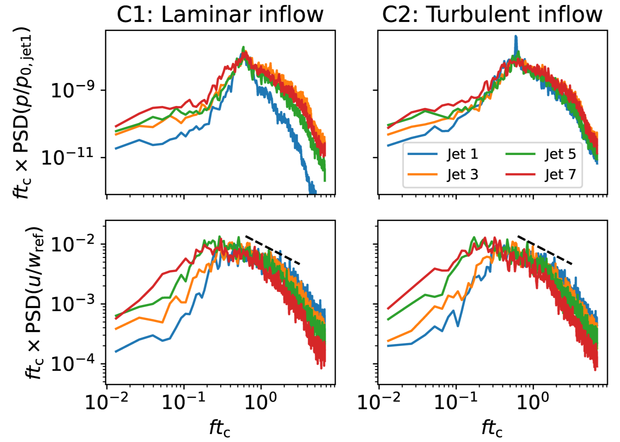

Fig. 10 Premultiplied power spectral density of pressure in jet shear layers at $(x_\mathrm{jet} + 0.3D, 3.5D)$ (*top*) and axial velocity u close to impingement wall above Nusselt maximum at $(x_\mathrm{Nu,max}, 0.2D)$ (*bottom*)

the jets are injected into the channel as laminar top hat profiles. Considering all these differences, the results seem consistent. A second comparison is shown with the results of Hossain et al. [9] at $\mathrm{Re}_\mathrm{jet} = 15\,000$ (triangles), whose configuration is also realized with one closed end and a cross flow driven by the jets only.[4] Since their channel height is only $3D$, the jet deflection is significantly lower. Their configuration also shows a strong increase in deflection after the third jet, which is consistent with their measured Nusselt number distribution. Stoy and Ben-Haim [36], on the other hand, show a non-linear best fit to experiments conducted at several jet Reynolds numbers with $H/D = 3.05$ and $L_y/D = 12$ (dotted line). Note that input data was sampled for single jets with incoming cross flow at velocity ratios between 0.13 and 0.4 and, hence, do not cover the low cross flow regime of our first four jets. Yang et al. [16] also report jet deflection over jet number $\mathrm{Re}_\mathrm{jet} = 15\,000$ (crosses). The relative cross sectional area of their cylindrical channel is roughly 2.5 times smaller than in our configuration leading to a stronger increase in cross flow velocity with jet number[5]. As above, due to the short distance to the impingement target of $3D$, the jet deflection grows significantly more slowly.

4 Unsteady dynamics

A first impression of the unsteady behavior under the developing cross flow is presented in Figure 9 by the temporal evolution of the spanwise-averaged Nusselt number $\langle \mathrm{Nu} \rangle_\mathrm{span}$ over the length of the channel for the case C2. The first three jets exhibit relatively minor oscillations of the Nusselt number primary and secondary maxima with slowly increasing amplitude from jet to jet. This plot allows to assess the direction in which flow structures travel by analyzing their slope. Here, structures moving both upstream (negative, e.g. white dashed line in inset lower right) and downstream (positive, e.g. black dashed lines) can be observed. Around jet four multiple qualitative changes can be found: First, upstream moving structures practically disappear, indicating, that the upstream wall jets cannot balance the existing cross flow in a spanwise-averaged sense. Second, as in the temporally averaged distribution (cf. Figure 7) no more secondary maxima can be observed. Finally, the oscillations increase more drastically from this point on. These changes correlate with the increased slope in jet deflection (cf. Figure 8). From jet 7 onwards, events can be observed in which very hot fluid (yellow) travels through the impingement region indicating a complete separation of the jet. Examples are marked with the black dashed lines. For jets 7 and 8, these occur rather sporadically at rates of about once every $200t_c$. The ninth jet, which lacks a downstream neighbor, separates at a much higher rate, in some instances with intervals below $20t_c$. To exclude these boundary effects in the further analysis, we will not consider jets 8 and 9 from here on.

Before analyzing larger scale organization in the flow, we need to identify the relevant frequencies. For this reason, Figure 10 shows the premultiplied power spectral density (PSD) below jets 1, 3, 5 and 7 in the shear layer at $(x_\mathrm{jet} + 0.3D, 3.5D)$ (*top*, marked with squares in Figure 4) and above the impingement point given by $(x_\mathrm{Nu,max}, 0.2D)$ (*bottom*, marked with circles in Figure 4). In the shear layer, the pressure p was used as a variable, while we plot the PSD of the axial velocity u close to the wall. The spectra were obtained using Welch's method [37] with a window of $76t_c$ and an overlap of 50%, allowing to resolve a minimal frequency of $0.0131/t_c$. We also compare the cases C1 with laminar inflow (*left*) and C2 with turbulent inflow (*right*). Within the jet shear layers, a clearly dominant peak can be found centered at the natural frequency of shear-layer instabilities of $\mathrm{St} = ft_c = 0.6$ [38]. Its amplitude is consistent over all jets and boundary conditions with the exception of jet 1 with turbulent inflow, which dominates the other jets of both cases by a factor of 4. With this notable exception, the peaks centered at this frequency are rather broad. Their width taken at a tenth of the peak value increases from 0.5 for jet 1 to 1.5 for jet 7 for case C1. Note that for the downstream jets, the high frequency flank of the peak becomes a part of the turbulent inertial range. For case C2 with turbulent inflow, in contrast, the width of the peaks remains relatively constant at 1.5, mainly, because jet 1 already shows a well-developed inertial range. Close to the impingement wall, in the spectrum of the axial velocity, this peak cannot be identified anymore. At high frequencies above 0.6, a turbulent spectrum can be found as indicated by the black dashed lines, representing a decay of the PSD proportional to $f^{-5/3}$. More interesting for the current investigation, however, is the lower end of the spectrum. Here, we can see a growth in amplitude over the jets up to an order of magnitude for frequencies below 0.1. This is a first indication of larger-scale, low-frequency organization in the flow with increasing cross flow ratio. Note, that the amplitudes are almost two orders of magnitude below the dominant jet vortex shedding and the connected largest turbulent structures. This will complicate the identification of such structures by pure investiga-

[4] Cross flow ratio estimated with $H/D = 3$, $L_y/D = 4$ and $r_0 = 0$.

[5] Cross flow ratio for the configuration of Yang et al. [16] estimated assuming a 240° circle segment for the channel cross section as

$$r(n) = r_0 + \frac{n\pi}{16\left(\frac{2\pi}{3} + \frac{\sqrt{3}}{4}\right)}$$

with $r_0 = 0$.

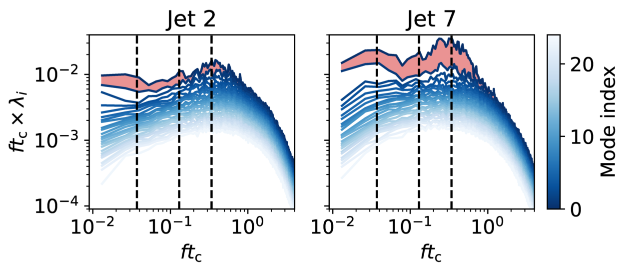

Fig. 11 SPOD premultiplied eigenvalues of velocity modes in plane $y = 0$ for jets 2 with low cross flow and 7 with high cross flow for case C2 with turbulent inflow

tion of eigenvalues obtained from modal analysis as they will not show clearly dominant peaks.

For the sake of clarity, we limit the following analysis to the case C2 with turbulent inflow. A Spectral Proper Orthogonal Decomposition (SPOD) [39–41] has been performed with a time series of fluctuating velocity $\mathbf{u}'$ using a turbulent kinetic energy (TKE) norm. We consider the plane $y = 0$ separately for jet 2 as the first jet experiencing low cross flow and jet 7 in a high-cross-flow environment. The data sets extend $\pm 2.5D$ around the jet center in axial direction and cover the complete channel height. The block size for Welch's method has been chosen as $76 t_c$ with 50% overlap as above.

Figure 11 shows the resulting premultiplied eigenvalues λ_i for all resulting modes with the area between the first two modes shaded in red to indicate potential low-rank behavior. As expected after the discussion above, no distinct peaks dominating by an order of magnitude stand out of the spectrum. Rather, we see that at frequencies below the turbulent inertial range, the first mode dominates by a maximum factor of roughly 1.5 for jet 2 while it dominates by a factor of 1.5 at low frequencies to a factor of 3 at $f t_c = 0.4$ for jet 7. We now select a low, medium and high frequency with large separation between the first two modes, marked by the vertical dashed lines. For each of these frequencies, we plot the respective first SPOD mode ϕ for all three velocity components u, v and w (indicated in the plots) in Figure 12. At medium and high (*middle* and *bottom*) frequencies, mode shapes can be found which are typical for vortex shedding [40]. They are most clearly visible in the u and w velocity components and follow the jet trajectory from the orifice to the impingement plate (A). Their intensity increases from with distance from the orifice before they are damped by the presence of the wall. Significant amplitudes in the spanwise component v are only found in jet 2 (B). For jet 7, the latter start to increase in amplitude at even higher frequencies around 0.6, which is not shown here. Note that the mode shapes are normalized and do not represent physical amplitudes. They have to be interpreted in combination with the respective eigenvalues (cf. Figure 11), which show that the first mode is roughly 2 times more energetic for jet 7 compared to jet 2 at the medium and high frequencies.

At the low frequency (Figure 12 *top*), larger structures can be identified. It has to be mentioned though, that these vary quite strongly with the chosen frequency as could be expected from the broadband nature of the spectrum. Independently of the frequency, however, they show large amplitudes mainly very close to the impingement wall in the axial velocity u (C) representing an axial oscillation of the stagnation point. The corresponding mode in the vertical velocity w shows the strongest modulation along at the upstream edge of the jet. While this structure extends from impingement wall to orifice for jet 2 (D), it is more closely bound to the near wall area $z/D < 2$ for jet 7 (E). Significant contributions from the spanwise velocity v can only be found for jet 7, where a large structure exists in the upper half of the channel (F), hinting at some kind of shedding of the cross flow behind the blockage of the jet itself. This is the clearly dominant effect in mode 2 at this frequency, which is not shown here due to space constraints. The Strouhal number for wake vortices behind a jet in cross flow at a comparable velocity ratio and Reynolds number was found to be around 0.13 by Fric and Roshko [42]. This corresponds to a non-dimensional frequency of $f t_c = 0.017$[6] with the cross flow ratio for jet 7 (cf. Figure 8). With the frequency resolution possible by our choice of block size, we cannot extract a mode for this frequency exactly but possibly see a first harmonic connected with this phenomenon at $f t_c = 0.04$. Yang et al. [17] offer a detailed discussion of this shedding mechanism driving the unsteadiness of the jets based on an unsteady RANS simulation.

As a final analysis, we turn to the temperature footprint of the jets on the impingement wall. The SPOD eigenvalue spectrum for the temperature T on sections of the wall under the single jets revealed that no high-frequency content can be found so close to the wall and that notable low-rank behavior could only be identified for $f t_c < 0.1$. Hence, we took a different approach for the wall data set and resorted to space-only Proper Orthogonal Decomposition (POD), which will give modes that can contribute a whole spectrum of frequencies to the complete signal. Again, we analyze subsets covering $\pm 2.5D$ around the jet centers, this time in both x- and y-direction.

Figure 13 shows the relative eigenvalues[7] $\lambda_{\mathrm{rel},i}$ of the first five POD modes for jets 1 to 7 analyzed separately and for jets 2-4 and 5-7 analyzed in combination, respectively. A first observation is that the relative eigenvalue of the first mode increases from 2.4% for jet 2 to 12.2% for jet 7. An exception is jet 4, which shows a reduced eigenvalue compared to the upstream one. Comparing the eigenvalues with the development of the maxima in the spanwise-averaged Nusselt number (cf. Figure 7) shows a correlation of Nusselt reduction with increasing eigenvalue of the first mode. This can be seen as a quantification of the argument that the Nusselt number distribution becomes more smeared by a more intense movement of the jet. This correlation also holds for the increase in the Nusselt maximum from jet 3 to 4. The contribution of the second mode increases up to jet 6 (with a slight drop for jet 3), where it dominates the third mode by a factor of 2.1. Jet 7, however, is dominated by mode 1 only. A spectral analysis of the POD time coefficients revealed that they are, indeed, associated with low frequencies only.

The corresponding shapes of the first three modes ϕ_T for jets 2 to 7 are shown in Figure 14.[8] In the low-cross-flow environment of jets 2 to 4, the primary movement of the jet leads to a spanwise variation of the surface temperature with low temperature at $y/D = -2$ in phase with high temperature at $y/D = 2$ and vice versa (A). Mode 2 primarily describes the temporal variation in the wall jet collision region about $1.5D$ to $2.5D$ upstream of the respective jet center (B) and is likely connected with an oscillation of the jet in the cross flow direction as this region shows a 180° phase shift compared to the downstream side of the jet (C). When the cross flow increases further, the shapes of mode 1 and 2 switch from jet 4 to 5. Now, the dominant mode is the axial oscillation of the temperature, while the spanwise oscillation corresponds to mode 2. Note, that the gap between modes 1 and 2 has reduced from jet 3 to 4 and is roughly constant for jets 4 and 5, which seems consistent with a change in dominant effects. While all previous mode shapes have been nearly symmetric about the $y = 0$ plane, jet 6 presents an exception as its modes 1 and 2 appear to be a mix

[6] We can write the Strouhal number as

$$\mathrm{St} = \frac{f\,D}{\langle \overline{u} \rangle_{\mathrm{bulk,channel}}} = f\,t_c \frac{w_{\mathrm{ref}}}{\langle \overline{w} \rangle_{\mathrm{bulk,jet}}} \frac{\langle \overline{w} \rangle_{\mathrm{bulk,jet}}}{\langle \overline{u} \rangle_{\mathrm{bulk,channel}}}.$$

[7] The relative eigenvalues

$$\lambda_{\mathrm{rel},i} = \frac{\sigma_i^2}{\sum_{j=1}^{N} \sigma_j^2}$$

can be obtained from a Singular Value Decomposition (SVD), which yields the singular values σ_i [43].

[8] Note that the sign of the complete mode can change without changing the meaning.

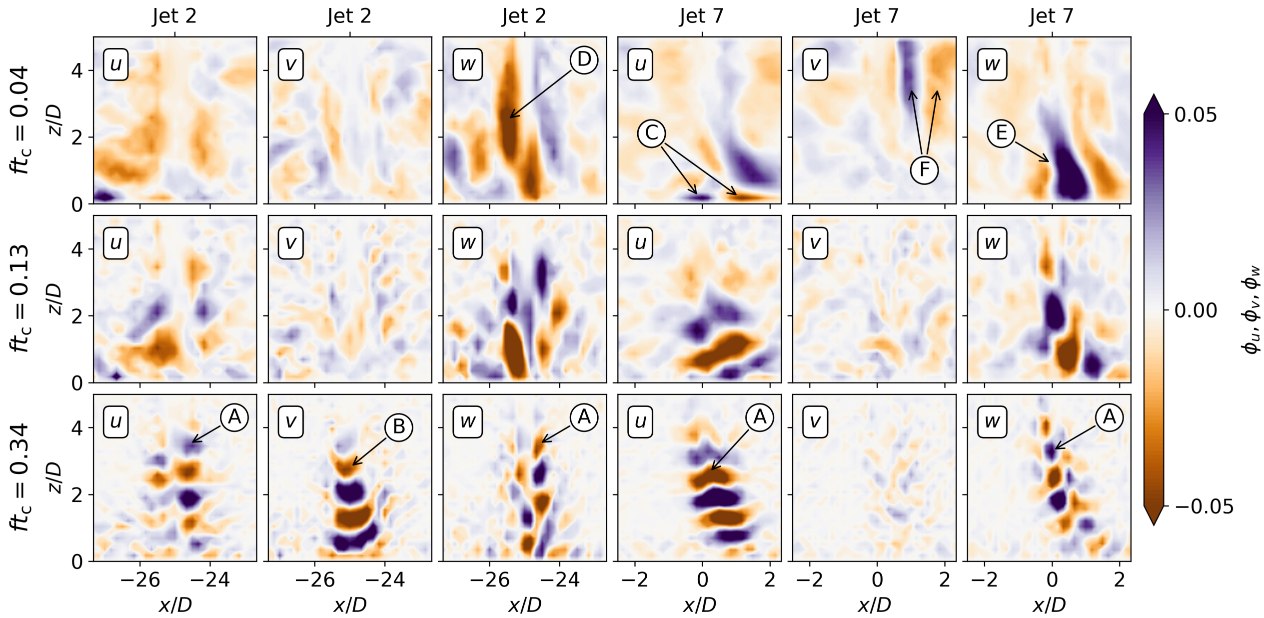

Fig. 12 First SPOD mode for velocity in plane $y = 0$ at low, medium and high frequency for jets 2 with low cross flow and 7 with high cross flow for case C2 with turbulent inflow

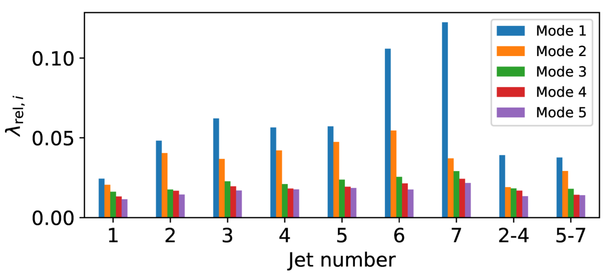

Fig. 13 POD relative eigenvalues $\lambda_{\mathrm{rel},i} = \sigma_i^2 \,/\, \sum_{j=1}^{N} \sigma_j^2$ of first five temperature modes on impingement wall evaluated for single jets and combinations for case C2 with turbulent inflow

of the axial and spanwise oscillations (D). With jet 7, the axial mode regains its dominance over the second mode with a factor of 3 such that most of the temperature variation can be attributed to axial oscillations (E). For the higher modes, for which mode 3 is shown as a representative, we see more complex patterns of combined axial and spanwise oscillations and their eigenvalues no longer dominate.

In order to investigate the interaction between the jets in different cross flow regimes, PODs of the wall data set with windows around jets 2-4 and jets 5-7, whose eigenvalues for the first five modes are also shown in Figure 13, have been performed. Compared to the analysis of the single jets, the first two modes combined contribute less to the total energy, with 5.8% and 6.7%, respectively. Figure 15 shows the shapes of the first three modes. First of all, traces of the mode shapes observed in the analysis of the single jets can be found here as well, but with the additional phase information over multiple jets showing non-negligible organization of the flow on large scales. In the low-cross-flow regime (*left*), a phase shift of 180° can be clearly identified between adjacent jets (e.g. (A)) with jets 2 and 4 swinging in phase in the spanwise direction (B). Consistently with the previous analysis, the second mode exhibits the largest amplitudes in the region where the wall jets collide. With jets 2 and 4 showing clear in-phase behavior in the high-temperature region (C), the data under jet 3 is relatively noisy, making it hard to judge if the respective region participates in this collective movement. Mode 3 is then the first to connect an axial oscillation behavior of jet 3 with a spanwise oscillation of jet 4 (D). This kind of combination becomes more dominant in the high-cross-flow regime (*right*). Here, the first mode combines the spanwise movement of jet 6 with the strong axial movement of jet 7 (E) while jet 5 is only weakly connected to this behavior via a spanwise mode shape at low amplitude in phase with jet 7 (F). Jet 5 also does not significantly participate in mode 2, which connects the axial oscillation of jet 7 with a stronger asymmetric motion of jet 6 (G). Mode 3 is the first mode with a significant contribution of jet 5 showing a similar shape as jet 6 in mode 2 with a high amplitude in the upstream region shifted towards the side wall and the corresponding area with 180° phase shift located downstream and at the opposite side wall (H). In summary, while the dominant modes in low cross flow do not show an interaction of axial and spanwise jet movement, the latter becomes the norm in high cross flow.

5 Conclusions

We have presented an LES-based analysis of the unsteady dynamics of a generic multi-jet impingement configuration consisting of nine jets spaced at five jet diameters, which inject fluid into a square channel of five jet diameters in height and width, heated on the impingement wall with constant heat flux. Compared to previously published results, which have validated the setup against PIV data, the present paper has introduced a modification to the inflow boundary conditions where synthetically generated resolved turbulence is considered. We presented a thorough analysis of the transient times of the simulation along with a 2D assessment of the statistical errors of the Nusselt number on the impingement plate. Although the influence of resolved turbulence at the inflow in terms of heat transfer characteristics was found to be minor, the follow-

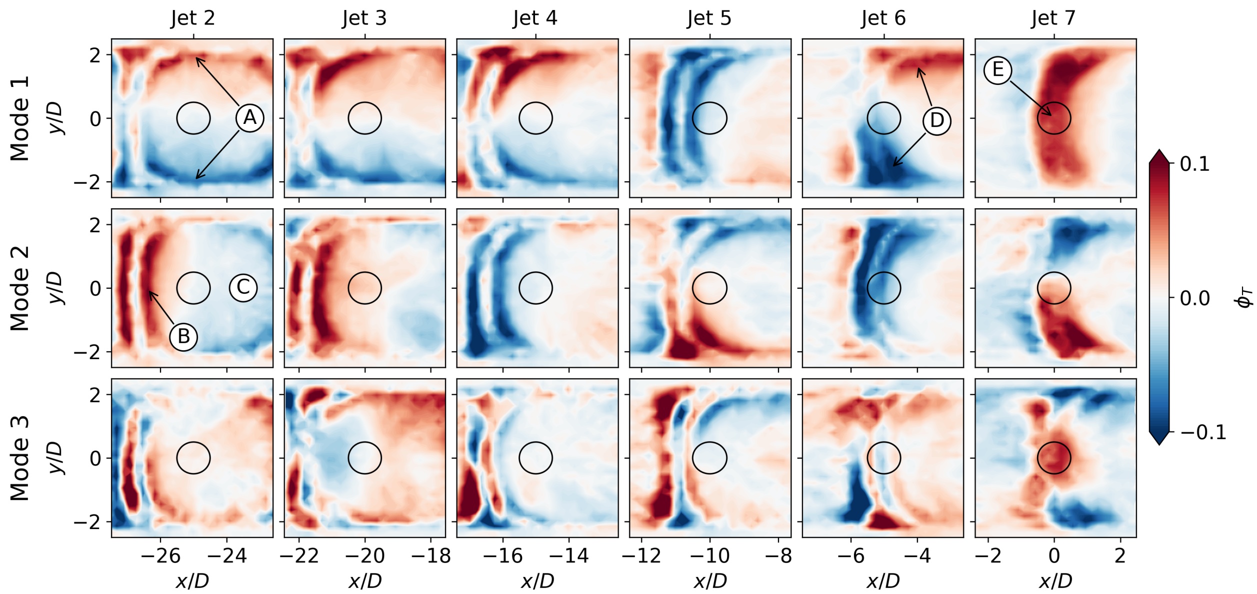

Fig. 14 First three POD modes of temperature T for single jets for case C2 with turbulent inflow

ing analysis has been conducted with this latest, in our view, more appropriate data set. We showed how the large-scale unsteadiness of the jets develops over the domain with increasing cross flow. Using POD and SPOD, we identified a low-cross-flow regime with a relative bulk velocity below 0.1 and a high-cross-flow regime between 0.1 and 0.2, between which the large-scale organization of the flow undergoes both a quantitative and a qualitative change. While the spanwise and axial oscillations of the jets were not connected in the low-cross-flow regime, more complex interactions of the neighboring jets could be identified with increasing cross flow. For further improvement of existing cooling systems a deep understanding of internal cooling flow characteristics essential. The presented analyses will support the design of more complex cooling configurations with additional geometric features in the channel aimed at utilizing or modifying the inherent large-scale unsteadiness of the flow. This study has already set a benchmark for future innovative configurations like the ArcConic turbulator [20]. This U-shaped device on the impingement plate enhances the jet flow by redirecting cross flow, which stabilizes the jet flow and reduces its unsteadiness. This stabilization results in a more uniform cooling throughout the system. Notably, it facilitates efficiency improvements, with the average Nusselt number increased by up to 16%. Especially at stagnation points, Nusselt number enhancements can reach up to 40%. Furthermore, the ArcConic ensures a uniform Nusselt number distribution, effectively preventing the degradation of downstream jets and contributing to an overall more efficient cooling process. Such novel configurations will be considered in more detail in future studies using unstructured high-order Discontinuous Galerkin (DG) discretization methods.

References

[1] Weigand, Bernhard and Spring, Sebastian. "Multiple Jet Impingement - A Review." *Heat Transfer Research* Vol. 42 No. 2 (2011): pp. 101–142.

[2] Barbosa, Flávia V., Teixeira, Senhorinha F.C.F. and Teixeira, José C.F. "Convection from multiple air jet impingement - A review." *Applied Thermal Engineering* Vol. 218 (2023): p. 119307. doi: 10.1016/j.applthermaleng.2022.119307.

[3] Dutta, Sandip and Singh, Prashant. "Impingement Heat Transfer Innovations and Enhancements: A Discussion on Selected Geometrical Features." *Volume 5B: Heat Transfer*: p. V05BT15A011. American Society of Mechanical Engineers. doi: 10.1115/GT2021-59394.

[4] Plant, Robert D., Friedman, Jacob and Saghir, M. Ziad. "A review of jet impingement cooling." *International Journal of Thermofluids* Vol. 17 (2023): p. 100312. doi: 10.1016/j.ijft.2023.100312.

[5] Shukla, Anuj and Dewan, Anupam. "Flow and thermal characteristics of jet impingement: Comprehensive review." *International Journal of Heat and Technology* Vol. 35 (2017): pp. 153–166. doi: 10.18280/ijht.350121.

[6] Zuckerman, N. and Lior, N. "Jet Impingement Heat Transfer: Physics, Correlations, and Numerical Modeling." *Advances in Heat Transfer* Vol. 39 (2006): pp. 565–631. doi: 10.1016/S0065-2717(06)39006-5.

[7] Dairay, T., Fortuné, V., Lamballais, E. and Brizzi, L.-E. "Direct numerical simulation of a turbulent jet impinging on a heated wall." *Journal of Fluid Mechanics* Vol. 764 (2015): p. 362–394. doi: 10.1017/jfm.2014.715.

[8] Wilke, Robert and Sesterhenn, Jörn. "Statistics of fully turbulent impinging jets." *Journal of Fluid Mechanics* Vol. 825 (2017): p. 795–824. doi: 10.1017/jfm.2017.414.

[9] Hossain, Jahed, Fernandez, Erik, Garrett, Christian and Kapat, Jayanta. "Flow and Heat Transfer Analysis in a Single Row Narrow Impingement Channel: Comparison of Particle Image Velocimetry, Large Eddy Simulation, and RANS to Identify RANS Limitations." *Journal of Turbomachinery* Vol. 140 No. 3 (2017): p. 031010. doi: 10.1115/1.4038711.

[10] Otero-Pérez, J. Javier, Sandberg, Richard D., Mizukami, Satoshi and Tanimoto, Koichi. "High-Fidelity Simulations of Multi-Jet Impingement Cooling Flows." *Journal of Turbomachinery* Vol. 143 No. 8 (2021): p. 081011. doi: 10.1115/1.4050446.

[11] Otero-Pérez, J. Javier and Sandberg, Richard D. "Compressibility and variable inertia effects on heat transfer in turbulent impinging jets." *Journal of Fluid Mechanics* Vol. 887 (2020): p. A15. doi: 10.1017/jfm.2020.5.

[12] Draksler, Martin, Ničeno, Bojan, Končar, Boštjan and Cizelj, Leon. "Large eddy simulation of multiple impinging jets in hexagonal configuration – Mean flow characteristics." *International Journal of Heat and Fluid Flow* Vol. 46 (2014): pp. 147–157. doi: 10.1016/j.ijheatfluidflow.2014.01.005.

[13] Draksler, Martin, Končar, Boštjan and Cizelj, Leon. "On the accuracy of Large Eddy Simulation of multiple impinging jets." *International Journal of Heat and Mass Transfer* Vol. 133 (2019): pp. 596–605. doi: 10.1016/j.ijheatmasstransfer.2018.12.125.

[14] Nguyen, Minh, Boussuge, Jean-François, Sagaut, Pierre and Larroya-Huguet, Juan-Carlos. "Large eddy simulation of a row of impinging jets with upstream crossflow using the lattice Boltzmann method." *International Journal of Heat and Mass Transfer* Vol. 212 (2023): p. 124256. doi: 10.1016/j.ijheatmasstransfer.2023.124256.

[15] Laroche, Emmanuel, Fenot, Matthieu, Dorignac, Eva, Vuillerme, Jean-Jacques, Brizzi, Laurent Emmanuel and Larroya, Juan Carlos. "A Combined Experimental and Numerical Investigation of the Flow and Heat Transfer Inside a Turbine Vane Cooled by Jet Impingement." *Journal of Turbomachinery* Vol. 140 No. 3 (2017): p. 031002. doi: 10.1115/1.4038411.

[16] Yang, Li, Ren, Jing, Jiang, Hongde and Ligrani, Phillip. "Experimental and numerical investigation of unsteady impingement cooling within a blade leading edge passage." *International Journal of Heat and Mass Transfer* Vol. 71 (2014): pp. 57–68. doi: https://doi.org/10.1016/j.ijheatmasstransfer.2013.12.006. URL https://www.sciencedirect.com/science/article/pii/S0017931013010508.

[17] Yang, Li, Ligrani, Phillip, Ren, Jing and Jiang, Hongde. "Unsteady Structure and Development of a Row of Impingement Jets, Including Kelvin–Helmholtz Vortex Development." *Journal of Fluids Engineering* Vol. 137 No. 5 (2015): p. 051201. doi: 10.1115/1.4029386.

[18] Rönnberg, Kristian and Duwig, Christophe. "Heat transfer and associated coherent structures of a single impinging jet from a round nozzle." *Inter-*

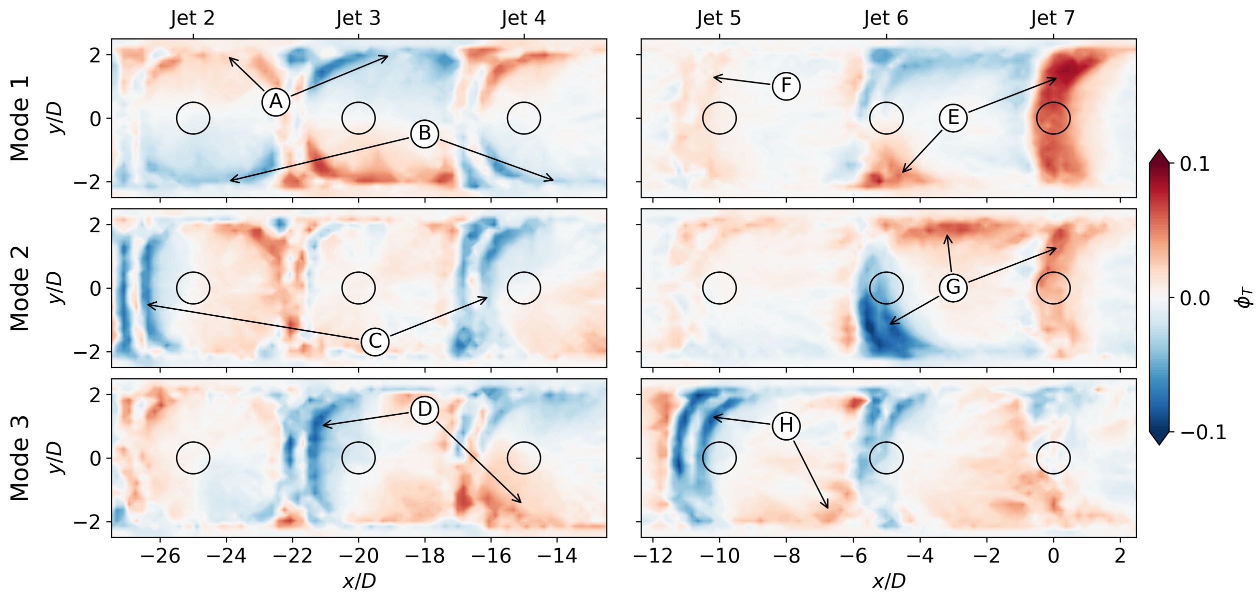

Fig. 15 First three POD modes of temperature T for jets 2-4 and jets 5-7 combined for case C2 with turbulent inflow

national Journal of Heat and Mass Transfer* Vol. 173 (2021): p. 121197. doi: 10.1016/j.ijheatmasstransfer.2021.121197.

[19] Tabassum, Sadiya, Hilfer, Michael, Brakmann, Robin G., Morsbach, Christian, Willert, Christian, Matha, Marcel and Schroll, Michael. "Assessment of Computational Fluid Dynamic Modeling of Multi-Jet Impingement Cooling and Validation With the Experiments." *Journal of Turbomachinery* Vol. 145 No. 7 (2023): p. 071005. doi: 10.1115/1.4056715.

[20] Brakmann, Robin G., Brose, Nina, Carvalho, Francisco, Chargui, Safae and Guarino, Roberto. "A Numerical Analaysis of Cross-Flow Reinforced Impingement Cooling with a U-Shaped Flow-Guide on the Hole Plate." *Volume 6B: Heat Transfer*. 2023. American Society of Mechanical Engineers. doi: 10.1115/GT2023-101097.

[21] Schlüß, D, Frey, C and Ashcroft, G. "Consistent Non-reflecting Boundary Conditions For Both Steady And Unsteady Flow Simulations In Turbomachinery Applications." *ECCOMAS Congress 2016 VII European Congress on Computational Methods in Applied Sciences and Engineering, Crete Island, Greece*. 2016. URL https://elib.dlr.de/111626/.

[22] van Leer, Bram. "Towards the ultimate conservative difference scheme. V. A second-order sequel to Godunov's method." *Journal of Computational Physics* Vol. 32 No. 1 (1979): pp. 101–136. doi: 10.1016/0021-9991(79)90145-1.

[23] Roe, P.L. "Approximate Riemann solvers, parameter vectors, and difference schemes." *Journal of Computational Physics* Vol. 43 No. 2 (1981): pp. 357–372. doi: 10.1016/0021-9991(81)90128-5.

[24] Shu, Chi-Wang and Osher, Stanley. "Efficient implementation of essentially non-oscillatory shock-capturing schemes." *J. Comput. Phys.* Vol. 77 No. 2 (1988): pp. 439–471. doi: 10.1016/0021-9991(88)90177-5.

[25] Nicoud, Franck and Ducros, Frédéric. "Subgrid-Scale Stress Modelling Based on the Square of the Velocity Gradient Tensor." *Flow Turbulence and Combustion* Vol. 62 (1999): pp. 183–200. doi: 10.1023/A:1009995426001.

[26] Morsbach, Christian and Bergmann, Michael. "Critical Analysis of the Numerical Setup for the Large-Eddy Simulation of the Low-Pressure Turbine Profile T106C." García-Villalba, Manuel, Kuerten, Hans and Salvetti, Maria Vittoria (eds.). *Direct and Large Eddy Simulation XII*: pp. 343–348. 2020. Springer International Publishing, Cham. doi: 10.1007/978-3-030-42822-8_45.

[27] Bergmann, M., Morsbach, C., Ashcroft, G. and Kügeler, E. "Statistical Error Estimation Methods for Engineering-Relevant Quantities From Scale-Resolving Simulations." *J. Turbomach.* Vol. 144 No. 3 (2021). doi: 10.1115/1.4052402. 031005.

[28] Fard afshar, Nima, Kozulovic, Dragan, Henninger, Stefan, Deutsch, Johannes and Bechlars, Patrick. "Turbulence anisotropy analysis at the middle section of a highly loaded 3D linear turbine cascade using Large Eddy Simulation." *Journal of the Global Power and Propulsion Society* Vol. 7 (2023): pp. 71–84. doi: 10.33737/jgpps/159784.

[29] Schroll, Michael, Klinner, Joachim, Müller, Martin, Matha, Marcel, Hilfer, Michael, Tabassum, Sadiya, Morsbach, Christian, Brakmann, Robin and Willert, Christian. "Experimental and Numerical Investigation of a Multi-Jet Impingement Cooling Configuration." *20th International Symposium on Application of Laser and Imaging Techniques to Fluid Mechanics*. 2022. URL https://elib.dlr.de/187567/.

[30] Shur, M. L., Spalart, P. R., Strelets, M. K. and Travin, A. K. "Synthetic Turbulence Generators for RANS-LES Interfaces in Zonal Simulations of Aerodynamic and Aeroacoustic Problems." *Flow Turbul. Combus.* Vol. 93 No. 1 (2014): pp. 63–92. doi: 10.1007/s10494-014-9534-8.

[31] Georgiadis, Nicholas J., Rizzetta, Donald P. and Fureby, Christer. "Large-Eddy Simulation: Current Capabilities, Recommended Practices, and Future Research." *AIAA Journal* Vol. 48 No. 8 (2010): pp. 1772–1784. doi: 10.2514/1.J050232.

[32] Fröhlich, Jochen, Mellen, Christopher P., Rodi, Wolfgang, Temmerman, Lionel and Leschziner, Michael A. "Highly resolved large-eddy simulation of separated flow in a channel with streamwise periodic constrictions." *Journal of Fluid Mechanics* Vol. 526 (2005): p. 19–66. doi: 10.1017/S0022112004002812.

[33] Ayachit, Utkarsh, Bauer, Andrew, Geveci, Berk, O'Leary, Patrick, Moreland, Kenneth, Fabian, Nathan and Mauldin, Jeffrey. "ParaView Catalyst: Enabling In Situ Data Analysis and Visualization." *Proceedings of the First Workshop on In Situ Infrastructures for Enabling Extreme-Scale Analysis and Visualization*. 2015. Association for Computing Machinery, New York, NY, USA. doi: 10.1145/2828612.2828624.

[34] K. Preston White, JR. "An Effective Truncation Heuristic for Bias Reduction in Simulation Output." *SIMULATION* Vol. 69 No. 6 (1997): pp. 323–334. doi: 10.1177/003754979706900601.

[35] Viskanta, R. "Heat transfer to impinging isothermal gas and flame jets." *Experimental Thermal and Fluid Science* Vol. 6 No. 2 (1993): pp. 111–134. doi: 10.1016/0894-1777(93)90022-B.

[36] Stoy, R. L. and Ben-Haim, Y. "Turbulent Jets in a Confined Crossflow." *Journal of Fluids Engineering* Vol. 95 No. 4 (1973): pp. 551–556. doi: 10.1115/1.3447069.

[37] Welch, P. "The use of fast Fourier transform for the estimation of power spectra: A method based on time averaging over short, modified periodograms." *IEEE Transactions on Audio and Electroacoustics* Vol. 15 No. 2 (1967): pp. 70–73. doi: 10.1109/TAU.1967.1161901.

[38] Hadžiabdić, M. and Hanjalić, K. "Vortical structures and heat transfer in a round impinging jet." *Journal of Fluid Mechanics* Vol. 596 (2008): p. 221–260. doi: 10.1017/S002211200700955X.

[39] Towne, Aaron, Schmidt, Oliver T. and Colonius, Tim. "Spectral proper orthogonal decomposition and its relationship to dynamic mode decomposition and resolvent analysis." *Journal of Fluid Mechanics* Vol. 847 (2018): pp. 821–867. doi: 10.1017/jfm.2018.283.

[40] Schmidt, Oliver T. and Colonius, Tim. "Guide to Spectral Proper Orthogonal Decomposition." *AIAA Journal* Vol. 58 No. 3 (2020): pp. 1023–1033. doi: 10.2514/1.J058809.

[41] Mengaldo, Gianmarco and Maulik, Romit. "PySPOD: A Python package for Spectral Proper Orthogonal Decomposition (SPOD)." *Journal of Open Source Software* Vol. 6 No. 60 (2021): p. 2862. doi: 10.21105/joss.02862.

[42] Fric, T. F. and Roshko, A. "Vortical structure in the wake of a transverse jet." *Journal of Fluid Mechanics* Vol. 279 (1994): p. 1–47. doi: 10.1017/S0022112094003800.

[43] Weiss, Julien. "A Tutorial on the Proper Orthogonal Decomposition." *AIAA Aviation 2019 Forum*. 2019. Dallas, Texas, USA. doi: 10.2514/6.2019-3333.

List of Figures

List of Tables